Journal of Industrial and Engineering Chemistry xxx (xxxx) xxx

Contents lists available at ScienceDirect

Journal of Industrial and Engineering Chemistry

journal homepage: www.elsevier.com/locate/jiec

Investigation of optimized spraying process for directly coated electrode in polymer electrolyte membrane fuel cell

Junghyun Lee [a,1], Haeun Lee [a,1], Ji Hoon Kim [a,c], Tuyet Anh Pham [d], Segeun Jang [b,*], Sang Moon Kim [a,*]

[a] Department of Mechanical Engineering, Incheon National University, Incheon 22012, Republic of Korea
[b] School of Mechanical Engineering, Kookmin University, Seoul 02707, Republic of Korea
[c] Research Institute of Basic Sciences, Incheon National University, Incheon 22012, Republic of Korea
[d] AHN Materials Inc, Incheon 22004, Republic of Korea

ARTICLE INFO

Keywords:
Optimized spray process
Spray coefficient
Critical ink flow rate
Membrane electrode assembly
Polymer electrolyte membrane fuel cell

ABSTRACT

Membrane electrode assembly (MEA) is a core component in polymer electrolyte membrane fuel cells (PEMFCs). A well-constructed catalyst layer is essential for achieving high-performance and reliable fuel cells. Among MEA fabrication processes, direct spray coating has advantages regarding cost-efficiency, processability, and controllability compared to direct sputtering and decal transfer method. In the spray process, the morphology of the catalyst layer depends on conditions in which ink droplets are sprayed and evaporated. Although quantitatively optimizing the spray process is crucial, there is still a lack of well-defined research for optimized spray process. Herein, we propose k-value that can indicate uniform coverage, expressed as a ratio of the area where ink droplets spread compared to the sprayed area. The k-1.0 MEA is fabricated under k-value conditions of one by adjusting nozzle moving speed, which is expected to have the most uniform coverage. Compared to k-0.3 MEA and k-3.0 MEA, the power density improves by 22.3 % and 11.1 %, respectively. This is attributed to the reduced ion transport resistance of the catalyst layer being reduced by 23.7 % and 8.5 % and the increased electrochemical active surface area by 16.1 % and 9.4 %, respectively. Furthermore, the morphology of catalyst layers and substrate temperature effect are investigated.

Introduction

As eco friendly-energy policies continue to strengthen worldwide and the demand for renewable energy rises, polymer electrolyte membrane fuel cells (PEMFCs) are emerging as prominent next-generation green energy power sources due to their zero-pollutant emission, low operating temperature, and high energy conversion efficiency [1–5]. Among the key components in PEMFCs, membrane electrode assembly (MEA) is a crucial component that serves as the site for both hydrogen oxidation and oxygen reduction reactions. Thus, MEA plays a decisive role in determining the overall performance of fuel cells [2,3,6]. Over the past few decades, there has been significant progress in the development of catalysts and electrolyte membranes [6–9], which has been crucial in improving fuel cell performance and characteristics. Along with selecting suitable materials, the construction of a catalyst layer with appropriate composition and configuration onto the electrolyte membrane is crucial in achieving high-performance and reliable fuel cells [10–12]. Diverse manufacturing processes, including direct sputtering, decal transfer, and direct spray coating, have been employed to build a catalyst layer on an electrolyte membrane [8,13–15]. In the case of direct sputtering, ultra-low loading 1D nanowhisker and tube structure have demonstrated outstanding characteristics [8]. However, large-area process and mass production through direct sputtering are limited. In the decal transfer process, a catalyst layer is initially coated on a decal substrate and subsequently transferred to a polymer electrolyte membrane under high pressure and high temperature above the glass transition temperature [16–18]. Although the decal transfer method appears suitable for large-scale production, it's important to note that the transfer of the catalyst layer can lead to structural deformation [16]. Meanwhile, the direct spray coating process involves directly coating the catalyst slurry onto the polymer electrolyte membrane using airbrushing or automatic spray devices, offering the advantages of

* Corresponding authors.
E-mail addresses: sjang@kookmin.ac.kr (S. Jang), ksm7852@inu.ac.kr (S.M. Kim).
[1] These authors contributed equally to this work.

https://doi.org/10.1016/j.jiec.2023.11.041
Received 16 August 2023; Received in revised form 5 November 2023; Accepted 17 November 2023
Available online 24 November 2023

processability and controllability. Compared to direct spray coating, decal transfer methods require a low surface energy substrate and a high ionomer content (ionomer to carbon support ratio of 0.8 or more) to achieve acceptable transfer yields [19,20]. However, a large amount of ionomer in the electrode can result in porosity reduction, catalyst poisoning, and an increase in oxygen transport resistance, which significantly impacts MEA performance [21,22]. Considering these points, it can be concluded that direct spray coating is desirable due to cost-efficiency, processability and controllability. While high controllability offers an advantage, it entails controlling multiple process variables such as substrate temperature, ink flow rate, nozzle speed, and carrier gas velocity. To achieve the desired high-quality MEA, optimization of spray conditions is necessary by finely tuning each process variable. In this study, we introduce a novel parameter, denoted as the k-value, which quantifies uniform coverage by expressing the ratio of the area where ink droplets spread to the total sprayed area. Specifically, the k-value represents the ratio of the ink droplet spread area to the entire sprayed region. The k-1.0 MEA was fabricated under conditions where the k-value is set to 1, ensuring the most uniform coverage possible. When compared to MEAs produced under k-value conditions of 0.3 and 3.0, the k-1.0 MEA exhibits a notable improvement in power density, respectively. These enhancements can be attributed to a reduction in ion transport resistance of the catalyst layer and an increased electrochemical active surface area. Furthermore, this study investigates catalyst layer morphology and substrate temperature effect on the MEAs.

Experimental section

Setup for automatic spray equipment

The cartesian-coordinated machine, gas-pressure controller, and vacuum hot plate were custom-made and integrated (Spray system Co.®, Republic of Korea). The gas pressure controller can adjust the air pressure from 0 to 0.5 MPa. In this study, the air pressure was consistently maintained at 0.05 MPa. The vacuum hot plate has a temperature setting range of room temperature to 150 °C. A syringe pump (LSP02-2A, LongerPump®, United Kingdom), syringe (KOVAX syringe 10 ml, KOREAVACCINE Co.,Ltd, Republic of Korea), and two-fluid nozzle (YM5JG4, Spray system Co.®, Republic of Korea) are installed to spray fluid. The linear motor speed of the syringe pump can be precisely adjusted within the range of 1 μm/min to 13 mm/min. In this study, 6 ml of catalyst ink was loaded into a 10 ml syringe and mounted on a syringe pump. The flow rate of the catalyst ink was set at 150 μm/min, which was accurately maintained and supplied to the two-fluid nozzle via a linear motor speed of 849 μm/min.

Preparation of the MEA

The catalyst ink solution sprayed on the cathode and anode was prepared by mixing 0.094 g Pt/C catalyst (40 % Platinum on Vulcan XC-72R, FC Catalyst, United States) and 5 wt.% Nafion ionomer solution (Sigma-Aldrich, United States). The loading weight ratio of the Nafion ionomer in the catalyst ink was set to 23 % of the total weight of the dried mixture (Pt/C + Nafion). In this process, 645 μL water and 18.8 ml isopropyl alcohol (IPA) were added to adjust the viscosity such that the nozzle would not get clogged during spraying. Moreover, the catalyst ink was homogenized by ultrasonication. An automatic spray machine was used to spray the catalyst ink onto both sides of a Nafion® 212 membrane (Sigma-Aldrich, United States) with a thickness of ~50 μm. The catalyst loading on both electrodes is of 0.2 mg_{Pt}/cm^2. The process was calibrated by comparing the weight of the polyethylene film before and after spraying. The prepared MEA, in which the catalyst layer was constructed, was dried for more than 12 h at room temperature before being assembled in a single cell.

Single cell assembly

The prepared MEA was placed between bipolar plates with a channel depth of 1 mm with gas diffusion layers (SGL GDL 39BB, SGL Carbon, Germany) and Teflon gaskets on both sides of the electrodes to prevent gas and water leakage. During the fastening process, eight bolts and nuts were tightened in a crisscross sequence with the sequential torque of 54, 81, and 108 N•m to prevent twisting the MEA.

Electrochemical measurements

We assembled MEAs with an active surface area of 5 cm^2 into a single cell and measured its performance. The temperature of the single cell was maintained at 70 °C under fully humidified conditions. Humidified hydrogen was supplied to the anode at a flow rate of 150 sccm, and humidified air was supplied to the cathode at a flow rate of 800 sccm. The electrochemical impedance spectroscopy (EIS) spectra were obtained using an impedance analyzer (HCP-803, BioLogic, France) under the same operating conditions to measure the ohmic resistance (R_{ohmic}) and kinetic resistance at the cathode ($R_{cathode}$) of PEMFC cells [23–26]. EIS was conducted at 0.5 V with an amplitude of 10 mV and frequency range from 0.1 Hz to 15 kHz [25,26]. The acquired EIS data were fitted through Z-VIEW s/w (Scribner Associates Inc., United States). Cyclic voltammetry (CV) was conducted to determine the electrochemical active surface area (ECSA) of the cathode [27,28]. The scanning rate was 50 mV/s under the range of 0.05 to 1.20 V. Measurement was carried out after purging the single cell by supplying fully humidified nitrogen gas at 25 °C. The fully humidified hydrogen gas was injected into the anode at a flow rate of 200 sccm and fully humidified nitrogen gas was injected into the cathode at a flow rate of 200 sccm for the analysis. In addition, EIS measurements were performed under the same conditions as the CV test to evaluate the protonic resistance across the catalyst layer (R_{CL}) [29,30]. The measurements were conducted at 0.2 V with an amplitude of 5 mV and frequency range from 70 mHz to 100 kHz. Additionally, we conducted acceleration stress test (AST) to evaluate durability of the catalyst layer of the fabricated MEAs. The durability test was performed in accordance with the U.S. Department of Energy protocol [31,32]. The AST was conducted under the condition of a triangle sweep cycle spanning from 1 V to 1.5 V, with a scan rate of 500 mV/s. This cycle was repeated 5000 times. During the AST, 200 sccm of fully humidified hydrogen and nitrogen into the anode and cathode electrodes were injected, respectively. The temperature and pressure were maintained at 70 °C and ambient pressure.

Physical analysis

We used a field-emission scanning electron microscope (FE-SEM; JSM-7001F, JEOL, Japan) with an acceleration voltage of 10.0 kV and an optical microscope (Olympus BX53MTRF-S, Japan) to observe the morphological characteristics of the MEAs fabricated in this study. Additionally, the pore size distribution of samples was characterized by using Brunauer-Emmett-Teller (BET) analyzer (TriStar II Plus, micromeritics, United States). Prior to BET analysis, the specimen was dehydrated and activated in a vacuum furnace at 120 °C for overnight condition. Nitrogen was used when measuring the adsorption (ADS) and desorption (DES) isotherms at ~196 °C. The BET relative pressure range (P/P_0) was 0 ~ 1. Pore size distributions (PSDs) were derived from the desorption branch using Barrett-Joyer-Halenda (BJH) method [33,34]. Also, we used a digital contact thermometer (GM1312, BENETECH, China) to measure the temperature of the polymer electrolyte membrane surface.

Results and discussion

Spray process setup

The custom-built spray equipment in this study comprises several components: a syringe pump, gas-pressure controller, two-fluid nozzle, and vacuum hot plate (Fig. 1**a** and **Fig. S1**). This system was designed to precisely deposit a liquid catalyst ink onto a target substrate, which is an electrolyte membrane. The syringe pump controls the flow rate of the liquid catalyst ink. The linear motor within the syringe pump was adjusted to finely regulate the flow rate, ensuring a controlled and consistent flow of the catalyst ink. The gas-pressure controller regulates the spray injection speed by adjusting the carrier gas-pressure. The two-fluid nozzle is a key component responsible for the atomization process. In particular, the liquid catalyst ink and carrier gas are injected into separate nozzle paths. The pressurized air flows through the air path in the nozzle, reducing the pressure at the front end of the liquid nozzle. High-speed gas atomizes the catalyst ink by breaking the liquid droplets, which are then directed toward the target substrate (Fig. 1**b**). The vacuum hot plate serves as a platform for holding the electrolyte membrane in place and promoting solvent evaporation in the deposited catalyst ink. After spraying, the catalyst ink is evaporated on the electrolyte membrane surface, preventing swelling and allowing for the formation of a catalyst-coated membrane (CCM).

In the spray process, atomized liquid droplets with a diameter of D_0 are initially emitted from the nozzle, while the carrier gas propels these droplets toward the substrate at the carrier gas velocity (V_0). Spherical droplets spread out and undergo deformation upon impact, forming circular two-dimensional thin sheets with a diameter of D_{max} on the substrate surface. The optimal spray process condition is achieved when a single spray spot area is completely covered with a diameter D_s without any overlap between the sprayed and impacted droplets on the substrate. In other words, it is crucial to ensure that there are neither excessive nor insufficient droplets on the substrate during the spray process. The formation of a uniform and well-distributed catalyst layer can be attained by carefully controlling the process parameters, thereby obtaining the optimal spray conditions.

The average D_{max}, which is the ink droplet size impacted on the surface, was measured by optical microscopy, as shown in Fig. 2**a**, to determine D_0 during the spray process. D_0 can be estimated through the following hydrodynamic relationship between D_0 and D_{max} with equilibrium contact angle, Reynolds number and Weber number in the previously published paper [35]:

$$\frac{D_{max}}{D_0} = \sqrt{\frac{We + 12}{3(1 - cos\theta) + 4(We/\sqrt{Re})}} (\text{Dimensionless}) \quad (1\text{-}1)$$

$$\text{Re} = \frac{\rho V_0 D_0}{\mu} (\text{Dimensionless}), \text{We} = \frac{\rho V_0^2 D_0}{\sigma} (\text{Dimensionless}) \quad (1\text{-}2)$$

where θ is the equilibrium contact angle of a liquid droplet on the substrate, σ is the surface tension of the liquid solution, μ is the viscosity of the liquid solution, and ρ is the density of the liquid solution. In the previous study, the authors experimentally investigated the effect of microdroplets on a smooth solid surface, and the above regime covers the transition between viscosity and surface tension dominated spreading of the droplets. To apply the equation, a droplet diameter(D_0) should satisfy a condition of 12 ~ 100 μm and a velocity (V_n) should satisfy the condition of 1 ~ 100 m/s [35]. Since the measured V_n and D_0 conform to the assumptions of previous studies, the use of that equation can be considered valid (Table 1). D_s is determined by measuring the width of the spray path when the nozzle sprays along a straight trajectory. It is essential to consider the movement of the spray nozzle to quantify the optimal spray process conditions because the MEA active surface area to be coated is larger than the cover of a single spray. Therefore, the spray nozzle needs to move periodically along a specific path to ensure uniform coverage. Considering the movement of the spray nozzle, we can determine the overall number of sprayed droplets (n) from the nozzle with a volume U. The duration (τ) with the required spray nozzle speed (V_n) for spraying on a unit spot area can be expressed as:

$$\tau = \frac{D_s}{V_n} \quad (2\text{-}1)$$

By determining τ, U is depicted using the relationship between ink flow rate(Q) and τ:

$$U = Q \bullet \tau = n\frac{4}{3}\pi D_0^3 \quad (2\text{-}2)$$

Under the assumption of uniformly sized and evenly distributed droplets over space, n is obtained as follows:

$$n = \frac{Q \bullet \tau}{\frac{4}{3}\pi D_0^3} \quad (2\text{-}3)$$

If the catalyst ink droplets can fully cover a single spray spot area without overlap, an optimal spray process is achieved. This is quantified by expressing the spray coefficient (*k*) as follows:

$$k = \frac{n(\frac{\pi}{4}D_{max}^2)}{\frac{\pi}{4}D_s^2} = n(\frac{D_{max}}{D_s})^2 \quad (2\text{-}4)$$

k provides a quantitative measure of the effectiveness of the spray process in achieving uniform coverage on the desired surface. A *k* value of 1 indicates that the substrate surface would be fully covered by the impacted droplet solution without overlapping regions, assuming a

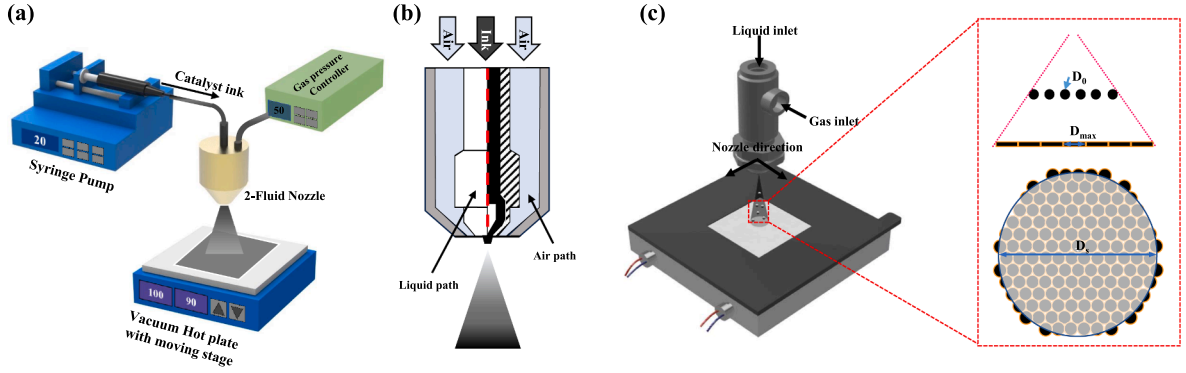

Fig. 1. (a) Schematic of the spray process of the catalyst ink onto the polymer electrolyte membrane. (b) Working principle of the two-fluid nozzle. Catalyst ink is pulled and sprayed out as pressurized air flows through the air path in the nozzle. (c) Schematic of the optimized spray process.

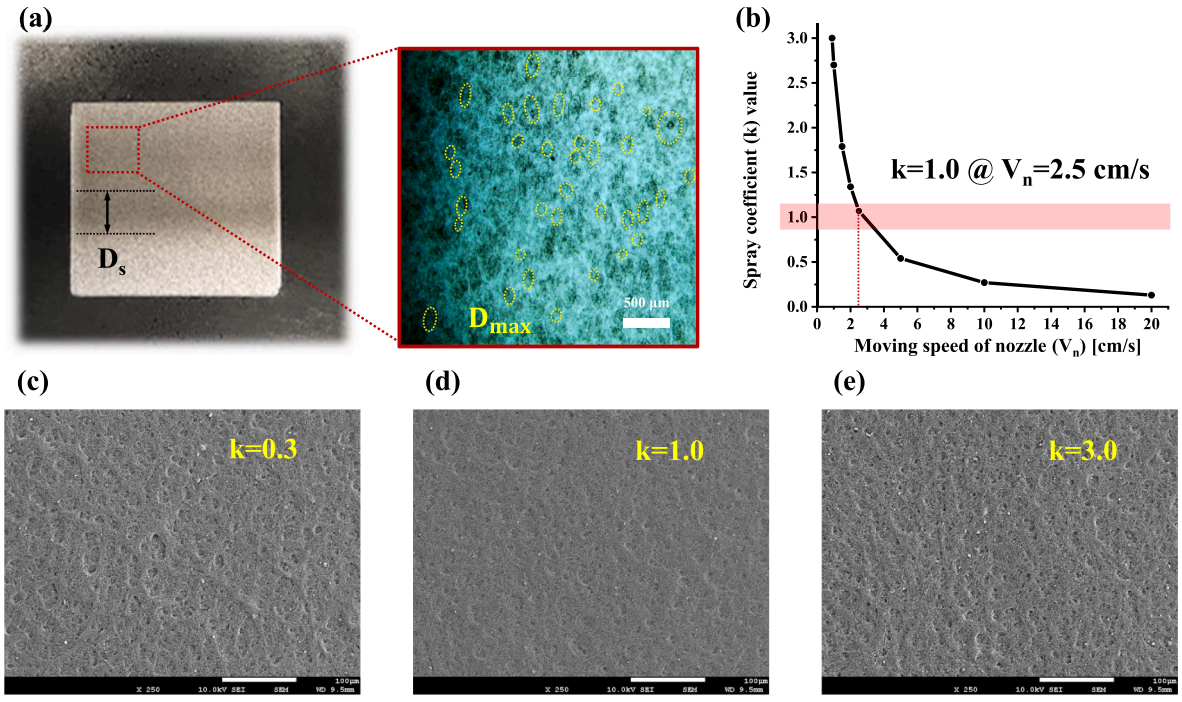

Fig. 2. (a) Digital camera image of the CCM after spraying the catalyst ink while the nozzle traversed the membrane in a straight line. The diameter of the single spray coverage area (D_s) is marked. The magnified region with an optical microscope image after a single spray in a straight line shows the diameters of a droplet impacting a surface (D_{max}). (b) Calculated spray constant depending on the moving speed of the spray nozzle. (c–e) SEM images of the surface morphology of the fabricated CCMs with *k* values of 0.3 (c), 1.0 (d), and 3.0 (e).

Table 1
Specific values of the experimental variables.

Q [m^3/s]	V_0 [m/s]	D_0 [m]	D_S [m]	D_{max} [m]	Θ [°]
~3.33 × 10^{-9}	~12	~3.467 × 10^{-5}	3.678 × 10^{-3}	~6.43 × 10^{-5}	0

uniform distribution of the droplets. A *k* value greater than 1 suggests that excessive droplets are spread on the substrate with overlap, which can lead to flooding. In contrast, a *k* value below 1 indicates that the amount of ink droplets cannot sufficiently cover a single spray spot area, which can result in incomplete coverage.

CCMs were fabricated with different *k* values of 0.3, 1.0, and 3.0 to verify the optimal spray process conditions. The process variables include the catalyst ink flow rate (Q), V_n, V_0, D_0, D_{max}, and D_s. Among these process variables, V_n, which has a wide adjustment range and allows accurate value setting, was set as the control variable. The remaining process variables were set as shown in Table 1, to ensure that the variables are within a reasonable range, considering the equipment setup. Considering the set variables, the *k* values were plotted as a function of V_n, as displayed in Fig. 2**b**. The graph reveals the V_n values of 0.9, 2.5, and 0.09 cm/s for *k* values of 0.3, 1.0, and 3.0, respectively.

Following the process conditions, MEAs with a catalyst loading of 0.2 mg/cm^2 were fabricated through the catalyst ink spray process. Each MEA was denoted as k-0.3 MEA, k-1.0 MEA, and k-3.0 MEA, following the corresponding *k* values. The surface of each MEA was observed by SEM, as shown in Fig. 2**c–e,** to confirm the surface morphology of the catalyst layer constructed on the membrane. For k-0.3 MEA and k-3.0 MEA, nonuniform, empty, and bumpy spaces, such as craters, were observed on the surface. For k-1.0 MEA, the surface was smooth and relatively uniform without a notable bump shape. The results suggest that the spray process condition for fabricating k-1.0 MEA inhibits flooding due to excessive droplets and surface irregularities by insufficient droplets to cover the sprayed area.

Polarization curves were obtained after constructing a single cell with MEAs to verify the electrochemical performances of the MEAs depending on the *k* values. The single cell performance was measured at 70 °C by supplying fully humidified H_2/Air. Fig. 3**a** indicates that k-1.0 MEA exhibits the highest performance with the maximum power density of 722 mW/cm^2, which is 22.4 % and 11.1 % higher than that of k-0.3 MEA (590 mW/cm^2) and k-3.0 MEA (650 mW/cm^2), respectively.

We conducted an EIS analysis at 0.5 V for each MEA under the same operating conditions for the performance measurements to elucidate the improved performance of k-1.0 MEA (Fig. 3**b**). **Fig. S2** shows the equivalent circuit of the PEMFC cathode electrode [24]. Each cell has an inherent resistance that causes voltage loss in charge flow. This is called R_{ohmic}, which is caused by the electrical resistance of fuel cell components and is expressed by the following equation [36]:

$$R_{ohmic} = R_{wc} + R_s + R_c \quad (3\text{-}1)$$

R_{wc} stands for uncompensated wire and contact resistance, R_s represents the resistance of cell components, and R_c signifies the contact resistance between cell components. The intercept of the high-frequency impedance loop with the real axis indicates a R_{ohmic}, representing ohmic losses within the fuel cell [37–39]. Also, in the equivalent circuit of the cathode, it is composed of $CPE_{cathode}$, which represents the positive phase element of the cathode, and R_{cahode}, which stands for reaction kinetics resistance of the electrochemical interface [39–41]. The measured EIS data were fitted using Z-View s/w. The analysis revealed that k-1.0 MEA exhibited a reduction in the R_{ohmic} by ~3.7 % and ~1.3 % and decrease in the $R_{cathode}$ by ~41 % and ~27 %, compared to k-0.3 MEA and k-3.0 MEA, respectively. These results suggest that the performance improvement is primarily attributed to a well-constructed catalyst layer with lower kinetic resistance, rather than the significant changes at the interface between the electrolyte membrane and catalyst layer.

We compared the ion-conduction characteristic through the catalyst layer using the transmission line model analysis (TLM). According to the model, a Warburg-like impedance at high frequencies corresponds to ion

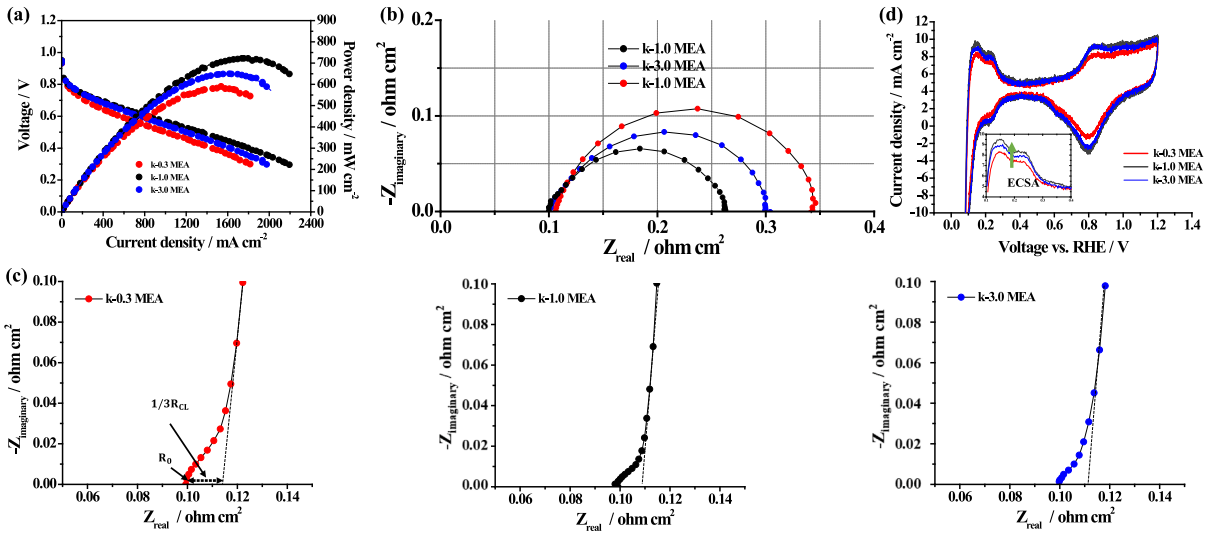

Fig. 3. (a) Polarization curves of k-0.3 MEA, k-1.0 MEA, and k-3.0 MEA at 70 °C with supplying fully humidified H_2/Air. (b) EIS measurements for the MEAs at 0.5 V under the same operating condition. (c) EIS measurements of a k-0.3 MEA, k-1.0 MEA, and k-3.0 MEA at 0.2 V under the operating conditions of 25 °C and RH100%. (H_2/N_2). (d) CV measurements for the MEAs.

migration through the catalyst layer, and a subsequent vertical spike at low frequencies to the total capacitance and resistance of the CL. The value for R_{CL} also can be calculated from the length of the Warburg-like region ($R_{CL}/3$) projected onto R_0 [29,30]. The TLM analysis is usually conducted in non-faradaic conditions at 0.2 V by supplying H_2/N_2 to the anode and cathode, respectively. This a different condition compared to EIS measurement under real fuel cell operating conditions under H_2/Air for calculating reaction kinetics resistance. Fig. 3**c** shows that the R_{CL} of k-1.0 MEA are ~24 % and ~8.5 % lower than that of k-0.3 MEA and k-3.0 MEA, respectively. This indicates that k-1.0 MEA enables a more efficient proton conduction due to the adequately dispersed catalyst particles and well-distributed ionomer network inside the catalyst layer.

We quantified the ECSA through CV measurements to corroborate our findings. The ECSA of the electrode can be calculated by applying the following equation:

$$ECSA = \frac{Q_T}{\Gamma \bullet L}(m^2/\mathrm{g}) \tag{4-1}$$

where Q_T is the integrated charge density (C/cm^2), L is the catalyst loading of the electrode (g/m^2), Γ is the specific charge required to oxidation/reduction (210 μC/cm^2 for platinum) [27,28]. Fig. 3**d** reveals that the ECSA value of k-1.0 MEA is ~16 % and ~9.4 % higher than that of k-0.3 MEA and k-3.0 MEA, respectively. This further confirms a well-distributed ionomer network within the catalyst layer in the MEA fabricated using the optimal spray process with the *k* of 1.0, thereby increasing the triple phase boundary. The representative values from the polarization curves, EIS, and CV measurement are summarized in Table 2. To further investigate the durability of the CL, the durability test was performed in accordance with the U.S. Department of Energy protocol [31,32,42]. **Fig. S3** shows that despite a performance reduction of approximately 15 % for all MEAs after AST, the k-1.0 MEA still exhibits the highest performance.

To quantify the morphology and characteristics of the catalyst layer, we obtained cross-sectional SEM images of the fabricated k-0.3, k-1.0, and k-3.0 MEAs. The measured thicknesses of CL for each MEA were 5.5, 6.4, and 7.1 μm for k-0.3, k-1.0, and k-3.0 MEAs (See Fig. 4).

And the calculated effective porosity of CL (ε_{cl}) using the following equation [43].

$$\varepsilon_{cl} = \frac{t_{cl} - t_0}{t_{cl}} \tag{5-1}$$

where t_{cl} (μm) is the height of CL, and t_0 (μm) is the estimated CL thickness when porosity is 0. And t_0 can be calculated using the following equation.

$$t_0 = \frac{m_{Nafion}}{\rho_{Nafion}} + \frac{m_{Pt}}{\rho_{Pt}} + \frac{m_{Carbon}}{\rho_{Carbon}}(\mathrm{cm}) \tag{5-2}$$

where m_i (g/cm^2) is mass per unit area for *i* material and ρ_i (g/cm^3) is density for *i* material. **Table S1** shows the variables for calculating t_0. The effective porosity of CL can be calculated using the equation above, and the results are shown in Table 3. A comparison with k-3.0 CL reveals that the effective porosity increased by 18 % and 5 % for k-0.3 CL and k-1.0 CL, respectively. In the case of k-3.0, where the excess liquid sprayed on the surface does not evaporate sufficiently, the effective porosity is the highest in the experimental samples. This phenomenon can be attributed to the broader spread of excess liquid in comparison to other

Table 2
Representative values from the polarization curves, EIS, and CV measurement.

MEA	I-V curve	EIS (H_2/N_2 at 0.2 V)		EIS (H_2/Air at 0.6 V)		CV Spectra
	*MPD (mW/cm^2)	R_0 (Ω•cm^2)	R_{CL} (Ω•cm^2)	R_{ohmic} (Ω•cm^2)	$R_{cathode}$ (Ω•cm^2)	ECSA (m^2/g$_{Pt}$)
k-0.3 MEA	590(−18.3 %)	0.1033(+4.1 %)	0.0426(+23.5 %)	0.1069(+3.9 %)	0.2410(+69.7 %)	25.04 (−13.8 %)
k-1.0 MEA	722(−)	0.0992(−)	0.0325(−)	0.1029(−)	0.1420(−)	29.06(−)
k-3.0 MEA	650(−9.9 %)	0.1016(+2.4 %)	0.0355(+9.2 %)	0.1043(+1.4 %)	0.1957(+37.8 %)	26.56 (−8.6 %)

* MPD: Maximum Power Density.

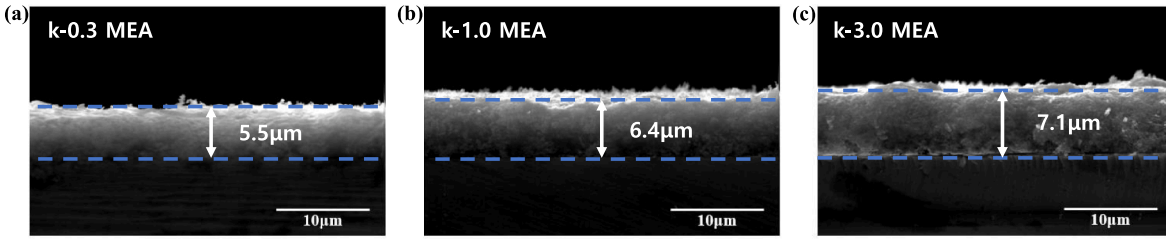

Fig. 4. SEM images of the cross-section morphology and CL height of the fabricated CCMs with k values of 0.3 (a), 1.0 (b), and 3.0 (c).

Table 3
Measured cathode electrode height of k-0.3, 1.0 and 3.0 MEA by SEM image and calculated effective porosity.

MEA	Pt loading [mg/cm^2]	CL thickness [μm]	effective porosity
k-0.3 MEA	0.2	5.5	0.55
k-1.0 MEA	0.2	6.4	0.62
k-3.0 MEA	0.2	7.1	0.65

samples caused by the applied force of air from the moving nozzle. Consequently, this leads to increased porosity and a thicker catalyst layer. Typically, higher porosity in the catalyst layer can lead to improved performance due to reduced mass transfer resistance. However, it's crucial to consider the potential impact of increased mass transfer resistance resulting from a more extended mass transfer pathway. As indicated in the transmission line model, an optimized pore structure within the catalyst layer is expected for efficient ion transport. Taking these factors into account, among the MEAs constructed in this experiment, the pore structure of the k-1.0 MEA is judged to be superior in terms of ion and mass transfer. Additional BET measurements were conducted to assess the pore structure of CL manufactured through the spray process. The pore size distribution of samples was characterized by BET analysis [33,34]. As depicted in **Fig. S4a**, the BET isotherm curves of all CLs exhibited typical mesoporous pore distribution characteristics [44]. Consequently, pore size distribution analysis was conducted using the BJH method. As shown in **Fig. S4b**, the pore diameter was measured to be in the range of 2–16 nm, and many relatively large pores of 4–12 nm were distributed in the order of k-3.0, k-1.0, and k-0.3. This is consistent with the results of the effective porosity previously observed and calculated. It's worth noting that the optimal condition does not necessarily mean having many or few large pores. Upon analysis, the k-1.0 MEA pore size distribution can be considered excellent in terms of ion transfer and mass transfer.

The effect of substrate temperature on the MEA morphology and fuel cell performance was investigated to further explore the optimized spray process conditions. When a spray droplet impacts the surface and immediately evaporates without flooding the membrane surface, the ideal temperature is achieved. This requires the heat transfer through the substrate to be greater than the heat required to instantly vaporize the spray droplets on the membrane surface. The heat transfer rate (q) from the substrate to the membrane is obtained as [45]:

$$q = -\kappa A_c \frac{\Delta T}{\Delta x}\,(\mathrm{W}) \tag{6-1}$$

where κ is the thermal conductivity coefficient of the membrane, A_c is the single spray spot area, Δx is the thickness of the membrane, and ΔT is the temperature difference between the top and bottom surface of the membrane. To measure the temperature at the bottom of the membrane, the temperature at the top of the parchment paper where the bottom surface of membrane contact together was measured. Next, to measure the temperature at the top of the membrane, the surface temperature was measured during the spray process. The substrate temperature was fixed at 50 °C, and the bottom and top surface temperatures of the membrane were measured to be 47 °C and 22 °C, respectively. During spray process, the sprayed solvent is absorbed through the electrolyte membrane surface, and additional heat energy is required to vaporize the liquid within the membrane, leading to a notable temperature difference between the area beneath and above the membrane. The detailed properties for the analysis are provided in **Table S2**.

Considering the thermal conductivity coefficient of Nafion, which is ~0.22 W/m·K [46], the calculated q is ~5.5 W. To calculate the critical flow rate (Q_c), the evaporation enthalpy of IPA (θ_{LV}) sprayed on the membrane surface was used. The q represents the heat energy transfer rate needed to evaporate the liquid from the membrane surface when catalyst ink is sprayed at a consistent flow rate at a substrate temperature of 50 °C. We can determine the Q_c (m^3/s) considering the θ_{LV} of ~39500 J/mol, IPA density (ρ_{IPA}) of ~786000 g/m^3, the IPA molar mass (M_{IPA}) of ~60.1 g/mol and mass flow rate $\dot{m}$ (g/s), as follows:

$$q(W) = \dot{m} \bullet \left(\frac{\theta_{LV}}{M_{IPA}}\right), \dot{m}\left(\frac{kg}{s}\right) = Q_c \bullet \rho_{IPA} \tag{6-2}$$

$$Q_C = \frac{q\hat{A}\cdot M_{IPA}}{\theta_{LV}\hat{A}\cdot\rho_{IPA}}(m^3/s) \tag{6-3}$$

The properties for IPA are provided in **Table S3**. Q_c is estimated to be ~150 μL/min when the temperature of the substrate is 50 °C. The results indicate that flooding can occur when the catalyst ink flow rate (Q) of 150 μL/min is higher than Q_c of ~45 μL/min during the spray process when the temperature of the substrate is 25 °C. In the previous experiment with different k values, MEAs were fabricated under a Q of 150 μL/min. The catalyst layer was well formed without flooding issues. We set the substrate temperatures to 25 °C and 80 °C while keeping a fixed Q at 150 μL/min to further investigate the impact of the substrate temperature. As the estimated Q_c at the substrate temperature of 80 °C is higher than 150 μL/min, the catalyst layer is expected to be well formed compared to that formed at a substrate temperature of 50 °C. However, at a substrate temperature of 25 °C, the Q_c value is less than 150 μL/min, suggesting an increased possibility of flooding. **Fig. S5** demonstrates the surface characteristics of the MEA fabricated at 80 °C, revealing a uniformly formed catalyst layer without noticeable surface inhomogeneity. In contrast, the MEA fabricated at 25 °Cdisplayed wrinkles on the entire surface (Fig. 5**b**), confirming the flooding and nonuniform expansion of the membrane. This occurs because the droplets sprayed on the surface do not evaporate immediately during the spray process. After confirming the morphological feature of the constructed catalyst layer on the membrane with varying substrate temperatures, the performance comparison of the fuel cells with three types of MEA samples (T-25 °C MEA, T-50 °C MEA, and T-80 °C MEA) was conducted. As shown in Fig. 5**c,** the T-50 °C MEA samples exhibited higher performances than the T-25 °C MEA which showed solvent flooding issues while showing similar performances with the T-80 °C MEA. But, the performance of the three types of samples did not show a significant difference. A minimal performance reduction of the T-25 °C MEA sample with severe electrode wrinkles is ascribed to the small active area of 5 cm^2 in this study. By considering the practical applications of PEMFCs, such as electric vehicles, that require a large active area of >250 cm^2 to secure high power output, the wrinkles in the electrode in large-area MEA samples can cause

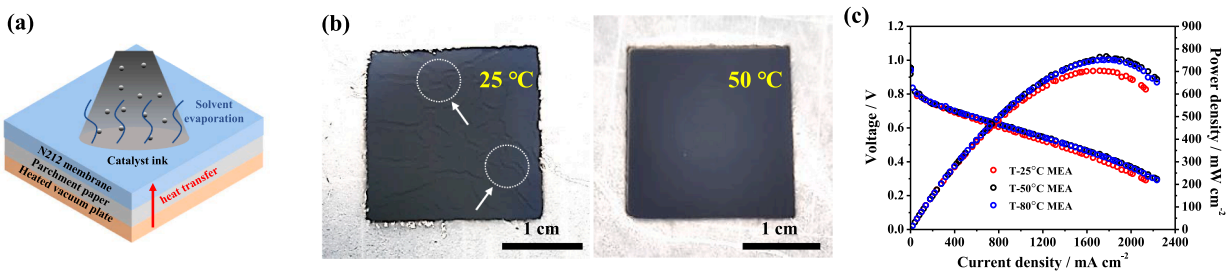

Fig. 5. (a) Scheme of the heat transfer phenomenon from the hot plate to the membrane surface and solvent evaporation of catalyst ink during the MEA spray fabrication process. (b) Camera images of the surface morphology of the MEA depending on the hot plate temperature at room temperature (25 °C) and 50 °C. (c) Polarization curves of T-25 °C MEA, T-50 °C MEA, and T-80 °C MEA at 70 °C with supplying fully humidified H_2/Air.

catastrophic failure in terms of durability and mass transport limitations [28,47]. Therefore, when manufacturing an MEA using a spray process, the Q_c corresponding to the substrate temperature should be considered together with the spraying condition, including the spreading characteristics of the spray droplet.

Conclusion

This study suggested the optimal conditions for constructing a catalyst layer on the membrane through the direct spray coating method. Based on a simple droplet spreading model, we introduced *k* as an indicator for achieving a uniformly deposited catalyst layer. *k* is defined as the ratio between covered area by the droplets and spray spot area. membrane electrode assemblies were manufactured under process conditions where k values were 0.3, 1.0, and 3.0. The MEAs were assembled into single cells and evaluated by measuring the polarization curve. The maximum power density of k-1.0 MEA increased by 22.4 % and 11.1 %, respectively, compared to k-0.3 and k-3.0 MEA. And the k-1.0 MEA exhibited lower reaction kinetic resistance at the cathode by ~41 % and ~27 % and lower ion transport resistance by ~24 % and ~8.5 %, compared to k-0.3 MEA and k-3.0 MEA through Faradaic and non-Faradaic EIS analysis, respectively. Furthermore, the ECSA value of k-1.0 MEA is ~16 % and ~9.4 % higher than that of k-0.3 MEA and k-3.0 MEA. The results indicate well-distributed ionomer network in CL of k-1.0 MEA was adequately formed, contributing to increasing the triple phase boundary and facilitating ion conduction through the catalyst layer. Moreover, through BET analysis and effective porosity measurements for each MEA, appropriate pore morphology was also investigated. Furthermore, the effect of the substrate temperature on the morphology of the MEA and fuel cell performance was investigated in terms of heat transfer. The Q_c corresponding to the substrate temperature was quantified. The calculated Q_c can serve as a standard for determining process temperature conditions, especially in situations where the solvent is excessively absorbed into the electrolyte membrane, leading to issues of flooding and wrinkles on the MEA. We believe our research can provide valuable insights into the fabrication of high-quality MEAs by optimizing the spray processing parameters, which further be adapted for other polymer electrolyte membrane-based electrochemical energy conversion devices, including water electrolysis and CO_2 reduction systems.

Declaration of competing interest

The authors declare that they have no known competing financial interests or personal relationships that could have appeared to influence the work reported in this paper.

Acknowledgment

This work was supported by the National Research Foundation (NRF) of Korea [grant number NRF- 2021M3H4A1A02042957]; and Incheon National University Research Grant in 2022 (2022-0001).

Appendix A. Supplementary material

Supplementary data to this article can be found online at https://doi.org/10.1016/j.jiec.2023.11.041.

References

[1] Z.-B. Wang, P.-J. Zuo, Y.-Y. Chu, Y.-Y. Shao, G.-P. Yin, Int. J. Hydrogen Energy 34 (2009) 4387–4394.
[2] E. Majlan, D. Rohendi, W. Daud, T. Husaini, M. Haque, Renew. Sustain. Energy Rev. 89 (2018) 117–134.
[3] S.E. Iyuke, A.B. Mohamad, A.A.H. Kadhum, W.R. Daud, C. Rachid, J. Power Sources 114 (2003) 195–202.
[4] U.H. Jung, K.T. Park, E.H. Park, S.H. Kim, J. Power Sources 159 (2006) 529–532.
[5] E.B. Agyekum, J.D. Ampah, T. Wilberforce, S. Afrane, C. Nutakor, Membranes 12 (2022) 1103.
[6] T. Maiyalagan, S. Pasupathi, in: Components for PEM fuel cells: An overview, pp. 143-189, Trans Tech Publ, 2010.
[7] Y. Guo, F. Pan, W. Chen, Z. Ding, D. Yang, B. Li, P. Ming, C. Zhang, Electrochem. Energy Rev. 4 (2021) 67–100.
[8] S. Jang, Y.S. Kang, D. Kim, S. Park, C. Seol, S. Lee, S.M. Kim, S.J. Yoo, Adv. Mater. (2022), 2204902.
[9] A. Baroutaji, A. Arjunan, A. Alaswad, A.S. Praveen, T. Wilberforce, M.A. Abdelkareem, A.-G. Olabi, 2020.
[10] R. Fernandez, P. Ferreira-Aparicio, L. Daza, J. Power Sources 151 (2005) 18–24.
[11] C.S. Kong, D.-Y. Kim, H.-K. Lee, Y.-G. Shul, T.-H. Lee, J. Power Sources 108 (2002) 185–191.
[12] S.-J. Shin, J.-K. Lee, H.-Y. Ha, S.-A. Hong, H.-S. Chun, I.-H. Oh, J. Power Sources 106 (2002) 146–152.
[13] S. Liu, S. Li, R. Wang, Y. Rao, Q. Zhong, K. Hong, M. Pan, J. Electrochem. Soc. 166 (2019) F1308.
[14] I. Farid, A. Boruah, J. Chutia, A.R. Pal, H. Bailung, Mater. Chem. Phys. 236 (2019), 121796.
[15] Z. Wei, K. Su, S. Sui, A. He, S. Du, Int. J. Hydrogen Energy 40 (2015) 3068–3074.
[16] S. Song, Z. Liang, W. Zhou, G. Sun, Q. Xin, V. Stergiopoulos, P. Tsiakaras, J. Power Sources 145 (2005) 495–501.
[17] G. Bender, T.A. Zawodzinski, A.P. Saab, J. Power Sources 124 (2003) 114–117.
[18] S. Srinivasan, Fuel Cells: From Fundamentals to Applications, Springer Science & Business media, 2006.
[19] T. Suzuki, S. Tsushima, S. Hirai, Int. J. Hydrogen Energy 36 (2011) 12361–12369.
[20] S.H. Akella, R.S. Sai Siddhardha, A. Ahire, N.K. Mal, Sci. Rep. 8 (2018) 12082.
[21] F. Zhou, Y. Yan, S. Guan, W. Guo, M. Sun, M. Pan, Int. J. Energy Res. 44 (2020) 10155–10167.
[22] F. Zhou, H. Zhang, S. Guan, G. Li, L. Xia, M. Pan, J. Catal. 414 (2022) 330–335.
[23] S. Asghari, A. Mokmeli, M. Samavati, Int. J. Hydrogen Energy 35 (2010) 9283–9290.
[24] A.M. Dhirde, N.V. Dale, H. Salehfar, M.D. Mann, T.-H. Han, IEEE Trans. Energy Convers. 25 (2010) 778–786.
[25] K. Dannenberg, P. Ekdunge, G. Lindbergh, J. Appl. Electrochem. 30 (2000) 1377–1387.
[26] J.W. Lim, Y.-H. Cho, M. Ahn, D.Y. Chung, Y.-H. Cho, N. Jung, Y.S. Kang, O.-H. Kim, M.J. Lee, M. Kim, J. Electrochem. Soc. 159 (2012) B378.
[27] E. Brightman, G. Hinds, R. O'Malley, J. Power Sources 242 (2013) 244–254.

[28] F.P. Lohmann-Richters, B. Abel, Á. Varga, J. Mater. Chem. A 6 (2018) 2700–2707.
[29] D. Malevich, B.R. Jayasankar, E. Halliop, J.G. Pharoah, B.A. Peppley, K. Karan, J. Electrochem. Soc. 159 (2012) F888.
[30] K.H. Oh, H.S. Kang, M.J. Choo, D.H. Jang, D. Lee, D.G. Lee, T.H. Kim, Y.T. Hong, J. K. Park, H.T. Kim, Adv. Mater. 27 (2015) 2974–2980.
[31] N. Macauley, D.D. Papadias, J. Fairweather, D. Spernjak, D. Langlois, R. Ahluwalia, K.L. More, R. Mukundan, R.L. Borup, J. Electrochem. Soc. 165 (2018) F3148–F3160.
[32] E. Padgett, V. Yarlagadda, M.E. Holtz, M. Ko, B.D. Levin, R.S. Kukreja, J. M. Ziegelbauer, R.N. Andrews, J. Ilavsky, A. Kongkanand, J. Electrochem. Soc. 166 (2019) F198–F207.
[33] R. Bardestani, G.S. Patience, S. Kaliaguine, Can. J. Chem. Eng. 97 (2019) 2781–2791.
[34] M. Hayati-Ashtiani, Part. Part. Syst. Char. 28 (2011) 71–76.
[35] C.W. Visser, Y. Tagawa, C. Sun, D. Lohse, Soft Matter 8 (2012) 10732–10737.
[36] P. Moçotéguy, B. Ludwig, D. Beretta, T. Pedersen, Int. J. Hydrogen Energy 45 (2020) 16724–16737.
[37] M. Grandi, K. Mayer, M. Gatalo, G. Kapun, F. Ruiz-Zepeda, B. Marius, M. Gaberšček, V. Hacker, Energies 14 (2021) 7299.
[38] C.-Y. Chen, K.-P. Huang, J. Appl. Electrochem. 48 (2018) 911–921.
[39] S. Jang, C. Seol, Y.S. Kang, S.M. Kim, S.J. Yoo, J. Power Sources 436 (2019), 226823.
[40] K. Darowicki, L. Gawel, Electrocatalysis 8 (2017) 235–244.
[41] R. O'hayre, S.-W. Cha, W. Colella, F.B. Prinz, Fuel Cell Fundamentals, John Wiley & Sons, 2016.
[42] J.H. Yeon, Y. Jang, M. Choi, S. Jang, ACS Appl. Mater. Interfaces 13 (2021) 56014–56024.
[43] X. Xie, G. Zhang, J. Zhou, K. Jiao, Int. J. Hydrogen Energy 42 (2017) 12521–12530.
[44] P. Samaddar, J. Hu, N. Barua, Y. Wang, T.-A. Lee, M.A. Prodanović, Z. Heidari, T. Hutter, ACS Omega 7 (2022) 43130–43138.
[45] T.N. Narasimhan, Rev. Geophys. 37 (1999) 151–172.
[46] L. Xian, Z. Li, S. Li, L. Chen, W.-Q. Tao, Int. J. Heat Mass Transf. 208 (2023), 124034.
[47] S. Kundu, M.W. Fowler, L.C. Simon, S. Grot, J. Power Sources 157 (2006) 650–656.